

# Molecular Simulation of Disjoining-Pressure Isotherms for Free Liquid, Lennard-Jones Thin Films

Divesh Bhatt, John Newman, and C. J. Radke\*

Department of Chemical Engineering, University of California, Berkeley, California 94720-1462

Received: January 23, 2002; In Final Form: April 12, 2002

We present canonical-ensemble molecular-dynamics simulations of disjoining-pressure isotherms in Lennard-Jones free liquid films. Thermodynamics demands that the disjoining pressure is determined uniquely as a function of the chemical potential purely from the phase diagram of the fluid. Our results from molecular dynamics validate this argument. The inverse-sixth-power distance term in the Lennard-Jones intermolecular potential represents van der Waals dispersion forces. Hence, we compare our results with classical Hamaker theory that is based on dispersion forces but assumes a slab geometry for the density profile and completely neglects fluid structure and entropy. We find that the Hamaker constant obtained from our simulations is about an order of magnitude larger than that from classical theory. To investigate the origin of this discrepancy, we calculate the disjoining-pressure isotherm using a density-functional theory relaxing the inherent assumptions in the Hamaker theory and imparting to the fluid an approximate structure. For disjoining pressure as a function of chemical potential, the results of density-functional theory and molecular dynamics are very close. Even for disjoining-pressure isotherms, and the subsequently calculated Hamaker constant, results of the density-functional theory are closer to the molecular-dynamics simulations by about a factor of 4 compared to Hamaker theory.

## Introduction

A thin liquid film on the order of a few nanometers in thickness and bounded on both the sides by air or vapor (and hence, a free liquid thin film) is of importance in systems, such as foams, where typical aqueous surfactant-stabilized films are surrounded by air. In thin liquid films, the normal component of pressure is constant across the interface, whereas the tangential component varies as a function of position perpendicular to the liquid/vapor interface.<sup>1–3</sup> However, the constant normal pressure in the film region is not the same as the isotropic pressure in the bulk liquid with which the film is in contact; the difference between these two pressures is the disjoining pressure,  $\Pi$ .<sup>2,3</sup> When reported as a function of film thickness  $h$ , at constant temperature,  $\Pi(h)$  is called the disjoining-pressure isotherm. Foam (and emulsion) stability is, in large part, determined by the disjoining-pressure isotherm.<sup>4,5</sup>

The classical thin-film theory of van der Waals forces, the Hamaker theory,<sup>6</sup> and also the more detailed theory of Lifshitz,<sup>7</sup> indicates that the disjoining pressure varies as the inverse cube of film thickness. However, in these theories, a slab model of the density profile is invoked. Thus, rigorous calculation of disjoining pressures requires detailed molecular simulations with physically real density profiles.

Numerous experimental studies are available for the disjoining-pressure isotherms of aqueous thin films containing surfactants,<sup>8–11</sup> and a few for aqueous films stabilized with proteins,<sup>12,13</sup> and polyelectrolytes.<sup>14</sup> Likewise, there are systematic molecular simulations studies in the literature<sup>15–18</sup> of

the forces in confined thin films (i.e., confined between solid walls). However, molecular simulations of the forces in free thin liquid films are almost nonexistent.<sup>19</sup> Long wavelength fluctuations (i.e., due to capillary waves) in systems with free interfaces tend to destabilize these metastable films.<sup>20</sup> Moreover, in the absence of a bounding surface, the liquid can evaporate (or the vapor can condense), making it difficult to maintain a liquid film during the course of a simulation.

We perform molecular-dynamics (MD) simulations of free thin liquid films to calculate the disjoining-pressure isotherm in a one-component liquid/vapor model system, with the intermolecular potential given by the well-known Lennard-Jones (LJ) potential. Although the LJ potential does not represent any real fluid exactly, it serves as a useful model because of the wealth of literature for LJ fluids. For a one-component LJ fluid, van der Waals dispersion forces<sup>21,22</sup> are present allowing direct comparison to Hamaker theory. However, disjoining pressures for these symmetric films are negative,<sup>6,22</sup> and the disjoining-pressure isotherm is positively sloping. As noted above, such purely attractive films are unstable to long wavelength fluctuations<sup>20</sup> and in real experiments cannot be studied. Fortunately, in computer simulation, the finite box size limits the long wavelength fluctuations. Nevertheless, evaporation/condensation processes remain a challenge to maintaining the film.

Density-functional theories for LJ systems have also been used quite extensively to study interfacial systems.<sup>23–25</sup> Here, we adopt a density-functional theory to calculate the disjoining-pressure isotherm for free thin LJ films. This exercise serves as a qualitative guideline to interpret the results from the molecular simulations, and also to evaluate the validity of the approximations made in both the density-functional and Hamaker theories.

\* To whom correspondence should be addressed. Phone: 510-642-5204. Fax: 510-642-4778. E-mail: radke@cchem.berkeley.edu.

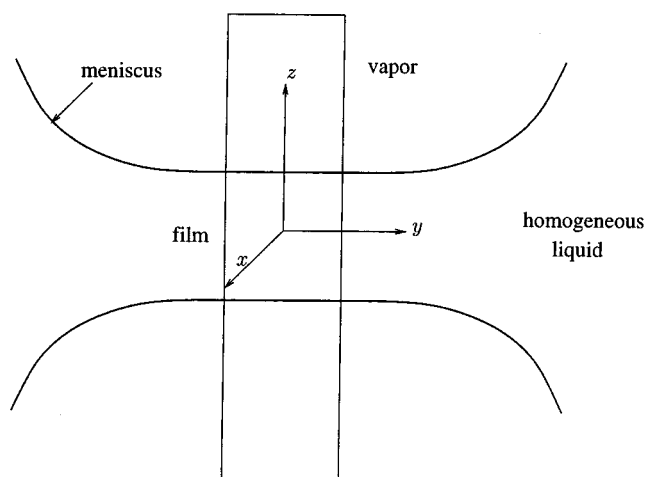


**Figure 1.** A schematic of the thin-film system. The film is in equilibrium with the bulk liquid connected to it via the Plateau-border meniscus (which is not included in the simulation). A vapor region surrounds the film on both sides.

## Simulations

**Methods.** In our simulations, the LJ potential is truncated and shifted at an interparticle separation of  $6.5\sigma$ , where  $\sigma$  is the LJ size parameter. Due to such a large cutoff, the properties of the fluid resemble closely those of the full LJ potential.<sup>26</sup> For this reason, we do not apply a tail correction to account for the interactions resulting from the neglected part of the intermolecular potential. Rather, the truncated and shifted potential is considered in its own right. A schematic of a two-dimensional projection of the thin-film system, for which the disjoining pressure is to be calculated, is shown in Figure 1. In the figure, a thin liquid film surrounded by vapor is shown connected to a bulk liquid through the Plateau-border meniscus that is not included in the simulation. For an LJ film, the disjoining pressure is negative, so the curvature of the Plateau-border meniscus is actually opposite to that shown. Figure 1 is drawn for illustration only. The liquid/vapor interface is perpendicular to the  $z$ -direction. Also shown in the figure is the simulation box, that is placed symmetrically over the flat part of the thin film. For each individual isothermal simulation, a slab of certain thickness (called the initial thickness) of particles corresponding to the coexistence liquid density is placed at the center of the box surrounded by particles corresponding to the coexistence vapor density. Periodic-boundary conditions are applied in all coordinate directions, and the minimum image convention is adopted. The length of the box in the  $x$ -direction is  $L_x = 14\sigma$ , in the  $y$ -direction is  $L_y = 14\sigma$ , and in the  $z$  direction is  $L_z = 40\sigma$ . Surface properties of an LJ fluid are not influenced by the system size as long as the dimensions parallel to the interface (i.e.,  $L_x$  and  $L_y$ ) are larger than about  $10\sigma$ .<sup>26,27</sup> Also, since  $L_z$  is much larger than the truncation distance of the LJ potential, the dependence of our results on  $L_z$  is expected to be negligible. Our chosen box size typically corresponds to about a thousand simulation particles. After allowing the system to equilibrate for 80,000 time steps (chosen so that the potential energy of the system and the density profile are statistically invariant), the production run of another 80,000 time steps is started (chosen so that we obtain a statistically significant averages). Each time step corresponds to 5 fs for argon, and the system is simulated in the NVT ensemble (using the Nose-Hoover Thermostat to maintain a constant temperature).<sup>28–31</sup> We accumulate averages during the production run.

As mentioned in the Introduction, the disjoining pressure is defined as

$$\Pi = p_N - p_L \quad (1)$$

where  $p_N$  is the normal pressure in the film and  $p_L$  is the pressure in the homogeneous liquid at the same chemical potential as the film (i.e.,  $p_L$  is the pressure in the homogeneous liquid constituting the constant-curvature part of meniscus). From eq 1, it is apparent that both the normal pressure and the chemical potential are the quantities of interest in calculating the disjoining pressure. We divide the simulation cell into small bins in the  $z$ -direction, perpendicular to the film/vapor interface, and calculate the normal component of the Irving and Kirkwood (IK) pressure tensor.<sup>32,33</sup> The size of the bins is varied, depending upon the film thickness, from  $0.2\sigma$  to  $0.5\sigma$ . Due to the finite size of the bin, we use the expression for the IK pressure tensor as mentioned by Weng et al.<sup>19</sup>

Once  $p_N$  is calculated, we establish  $p_L$  at the same chemical potential as in the film. To accomplish this, we follow the prescription suggested by Winter,<sup>34</sup> and use the one-component Gibbs–Duhem equation at constant temperature

$$dp_L = \rho_L d\mu \quad (2)$$

where  $\rho_L$  is the density of the homogeneous liquid, and  $\mu$  is the chemical potential. Now, we assume that the liquid density does not vary with pressure (or with the chemical potential), and we integrate eq 2 from the state of bulk liquid/vapor coexistence (the saturation state) to the condition of the liquid in the meniscus (that is in equilibrium with the film) with the result

$$p_L - p_{\text{sat}} = \rho_L(\mu - \mu_{\text{sat}}) \quad (3)$$

where  $p_{\text{sat}}$  is the vapor pressure in the saturation state and  $\mu_{\text{sat}}$  is the saturation chemical potential. Appendix A establishes that the error due to the assumption of constant  $\rho_L$  is negligible.

To obtain the isothermal saturation state, we simulate a thick film corresponding to the bulk liquid/vapor coexistence point. Thus, from eq 3,  $p_L$  at the chemical potential of the film is known, and the disjoining pressure follows in a straightforward manner from eq 1. Chemical potentials required for both the film and the reference saturation system are calculated using Widom's method for inhomogeneous systems.<sup>35</sup> Here, again, we divide the simulation cell into bins perpendicular to the interface. In this case, the size of the bins is not important. We choose the bin sizes to be  $1.0\sigma$ , larger than those used to calculate  $p_N$ , and we accumulate the averages of the chemical potential in the vapor part of the cell only (since the ghost particle insertion in Widom's method works well for low-density fluids, and the larger bin size allows for more accuracy). Simulation temperatures are chosen to be around 0.9 in reduced LJ units (the critical point of an LJ fluid is 1.316<sup>36,37</sup> and the triple point is approximately 0.69<sup>36</sup>). At temperatures closer to the critical point, it is increasingly difficult to maintain metastable films. Temperatures closer to the triple point require much longer runs. Before presenting the results of the MD simulations, we briefly highlight some important physical aspects of our work.

**Thermodynamics.**  $\mu$  is graphed as a function of  $p$  in Figure 2 for an LJ fluid calculated from the analytic equation of state (EOS) of Johnson et al.<sup>36</sup> More specifically,  $\mu^* - T^* \ln \Lambda^*$  is plotted as a function of  $p^*$ , where the superscript “\*” denotes a nondimensional quantity using the LJ parameters  $\epsilon$  and  $\sigma$ , and where  $\Lambda^*$  is the nondimensional thermal de Broglie wavelength. Since we are concerned with isotherms only, the

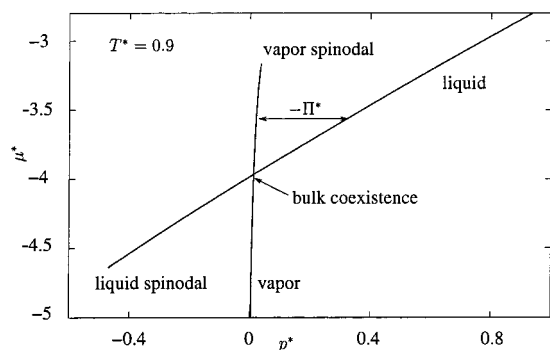


**Figure 2.** The  $\mu$ - $p$  phase diagram for a Lennard-Jones fluid at  $T^* = 0.9$ . Liquid and the vapor lines are shown, along with the spinodal points where they, respectively, terminate. A particular value of the disjoining pressure is also shown by a double-sided arrow for illustration.

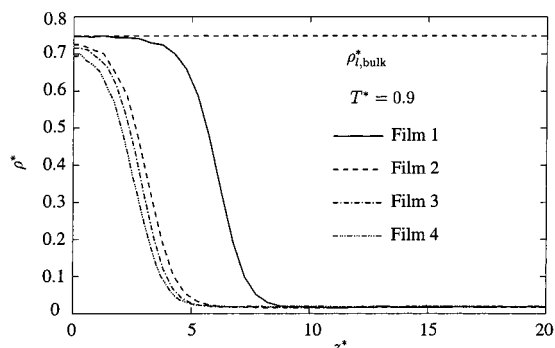


**Figure 3.** Density profiles from MD simulations for four different film thicknesses at a reduced temperature of 0.9. The bulk-coexistence liquid density is also shown.

thermal de Broglie wavelength need not be specified. From this point onward, we replace  $\mu^*$  by  $\mu^* - T^* \ln \Lambda^*$ , and we use the symbol  $\mu^*$  to designate this difference.

The point in Figure 2 where the liquid and the vapor lines (shown by solid lines) cross is the bulk coexistence point. The liquid and vapor lines each terminate at one end, which are the spinodal points. Due to the extended vapor region surrounding the film, the normal pressure and the chemical potential of the film are identical, respectively, to the corresponding isotropic pressure and chemical potential in the extended vapor region. Thus,  $p_N$  and  $\mu$  of the film must lie on the homogeneous vapor line in Figure 2. For a given chemical potential of the thin film, the pressure (for the same chemical potential) in the homogeneous, Plateau-border liquid follows directly from that on the liquid line in Figure 2. As an illustration,  $\Pi^*$  is shown at a particular  $\mu^*$  ( $= -3.60$ ) in Figure 2. In other words,  $\Pi$  as a function of  $\mu$  is determined as the difference between the pressures in the vapor and liquid phases at the same chemical potential. Accordingly,  $\Pi$  is obtained as a function of  $\mu$  purely from the phase diagram. However, to establish the disjoining-pressure isotherm,  $\Pi(h)$ , we need the film density profiles (i.e., to establish the film thickness). Note that, for a LJ system, the disjoining pressure is negative so that the vapor phase surrounding the film resides along the vapor line above the bulk-phase coexistence point. We now quantify these ideas using molecular dynamics.

## Results and Discussion

**Molecular Simulations.** Figure 3 reports four different simulated density profiles as a function of  $z^*$  at a reduced temperature of  $T^* = 0.9$  where the center of the simulation box

is at  $z^* = 0$ . The number of atoms  $N$  in the simulation box for film 1 is 1851. For film 2,  $N = 984$ ; for film 3,  $N = 912$ ; and for film 4,  $N = 839$ . These films correspond to initial slab film thicknesses (as defined earlier),  $h_i$ , of  $12\sigma$  for film 1,  $6\sigma$  for film 2,  $5.5\sigma$  for film 3, and  $5\sigma$  for film 4.

Film 1 is thick, closely corresponding to bulk liquid/vapor coexistence. Here,  $\Pi$  equals zero within the precision of our calculation. This is clear because the density at the center of the film reaches the bulk liquid density  $\rho_{l,bulk}^* = 0.752$ . Films 2–4, however, are thin films for which the centerline densities fall below the bulk liquid density. As reported in the fourth column of Table 1 and is clear from Figure 3, this effect is increasingly more pronounced as the films become thinner. Although not apparent from the scale of the figure, these films have higher densities in the vapor region than does film 1 (that has a vapor density corresponding to bulk coexistence at the set temperature). The fifth column of Table 1 shows  $\rho_v^*$  for films 1–4. Films thinner than film 4 breakup in the simulation, whereby the two liquid/vapor interfaces collapse at certain points on the  $x$ - $y$  plane, similar to that previously observed in the literature.<sup>19</sup> As an aside, we note here that a film of initial thickness  $4.5\sigma$  ruptures. However, films between  $4.5\sigma$  and  $5\sigma$  (film 4) in initial thickness might remain stable during simulation.

To demonstrate that the normal pressure is constant across the thin-film interfaces, we plot  $p_N^*$  as a function of  $z^*$  in Figure 4 for film 3 at  $T^* = 0.9$ . As is evident from the dot-dashed line in the figure,  $p_N^*$  does indeed remain constant across the film. All other simulated films here also show a similar constancy of the normal pressure. In more detail, the kinetic part of the normal pressure ( $p_{N,k}^* = \rho^* T^*$ ) is shown as a solid line in Figure 4, and the intermolecular part ( $p_{N,i}^*$ ) is shown as a dashed line. Both  $p_{N,k}$  and  $p_{N,i}$  are higher in the liquid part of the thin film because of the higher density of particles. The difference between the two is  $p_N$ .

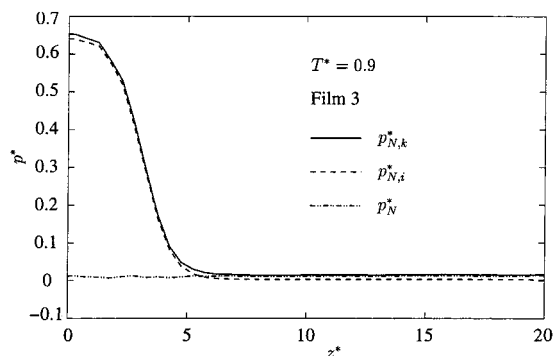
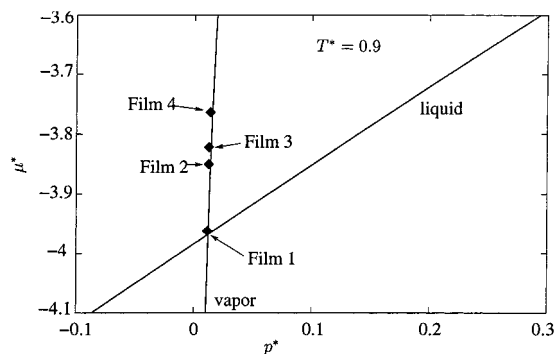
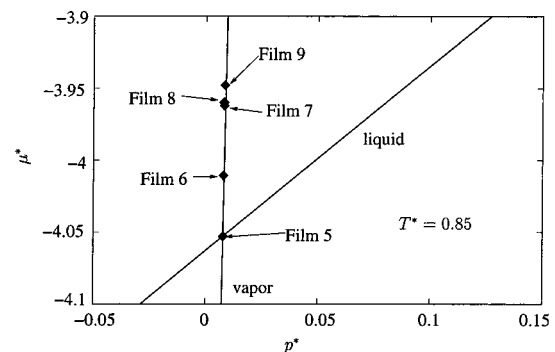
The sixth and the seventh columns of Table 1 report the normal pressures and the chemical potentials calculated for the four films from the simulations at  $T^* = 0.9$ . As the film thins, the normal pressure and the chemical potential increase. This result is in accord with the observation made earlier that the vapor in the simulation box increases in density as the film thins.

Figure 5 locates the films on the  $\mu^*$ -versus- $p^*$  phase diagram for an LJ fluid. Solid lines are the same as those in Figure 2, and the simulated films are indicated by closed diamonds. As clear from Figure 5, film 1 corresponds to the bulk coexistence point, and  $\Pi \approx 0$ . Films 2–4 fall on the homogeneous vapor line, as anticipated. Similarly, Figure 6 shows films 5–9, as closed diamonds, on the phase diagram for  $T^* = 0.85$ . Film 5 ( $N = 1877$ ,  $h_i^* = 12.0$ ) corresponds to bulk coexistence, whereas films 6 ( $N = 976$ ,  $h_i^* = 6.0$ ), 7 ( $N = 901$ ,  $h_i^* = 5.5$ ), 8 ( $N = 826$ ,  $h_i^* = 5.0$ ), and 9 ( $N = 796$ ,  $h_i^* = 4.8$ ) are thin films. These films are initially prepared in the same manner as films 1–4 with bulk-coexistence densities determined from the LJ EOS<sup>36</sup> and a slab of the coexistence liquid density placed in the center of the simulation box. Solid lines in Figure 6 are, again, obtained from the LJ EOS,<sup>36</sup> and the properties of films 5–9 are summarized in Table 1.

Calculation of the disjoining pressure for the thin films follows by the method outlined earlier. With the knowledge that the bulk liquid density in the center of film 1 is 0.752 at  $T^* = 0.9$ ,  $\Pi^*$  for film 1 is calculated from eqs 1 and 3 as 0, for film 2,  $\Pi^* = -0.088$ ; for film 3,  $\Pi^* = -0.107$ ; and for film 4,  $\Pi^* = -0.152$ . Similarly, the liquid density in the center of film 5 (the bulk coexistence density at  $T^* = 0.85$ ) is 0.776. This leads

**TABLE 1: Relevant Simulated Quantities of All the Films at Both  $T^* = 0.9$  and 0.85**

film	$N$	$T^*$	$\rho_1^*(z^* = 0)$	$\rho_v^*$	$p_N^*$	$\mu^*$	$\Pi^*$	$h_i^*$	$h^*$
1	1851	0.9	0.752	0.0150	0.01137	-3.9620		12.0	12.0
2	984	0.9	0.725	0.0173	0.01235	-3.8501	-0.088	6.0	5.82
3	912	0.9	0.715	0.0185	0.01246	-3.8217	-0.107	5.5	5.25
4	839	0.9	0.695	0.0196	0.01364	-3.7635	-0.152	5.0	4.67
5	1877	0.85	0.776	0.0097	0.0077	-4.0530		12.0	12.0
6	976	0.85	0.753	0.0103	0.00782	-4.0107	-0.0320	6.0	5.94
7	901	0.85	0.745	0.0110	0.00807	-3.9622	-0.0693	5.5	5.39
8	826	0.85	0.730	0.0110	0.00797	-3.9600	-0.0717	5.0	4.89
9	796	0.85	0.722	0.0112	0.00832	-3.9480	-0.0807	4.8	4.68

**Figure 4.** The normal component of the pressure tensor  $p_N^*$  (dot-dashed line) as a function of  $z^*$  for film 3. The kinetic ( $p_{N,k}^*$ ), solid line, and the intermolecular ( $p_{N,i}^*$ ), dashed line, contributions to the normal pressure are also shown.**Figure 5.** Films 1–4 on the  $\mu^*$ -versus- $p^*$  plot of an LJ fluid at  $T^* = 0.9$ , shown as closed diamonds. The horizontal distance between the points and the liquid line gives the negative value of the disjoining pressure.**Figure 6.** Films 5–9 on the  $\mu^*$ -versus- $p^*$  plot of an LJ fluid at  $T^* = 0.85$ , shown as closed diamonds. The horizontal distance between the points and the liquid line gives the negative value of the disjoining pressure.

to the values of the disjoining pressures as  $\Pi^* = -0.032$  for film 6,  $\Pi^* = -0.0693$  for film 7,  $\Pi^* = -0.0717$  for film 8, and  $\Pi^* = -0.0807$  for film 9. These values of  $\Pi^*$  are shown in the eighth column of Table 1.

**Film Thickness.** Disjoining pressure is reported in the literature as a function of a slab film thickness. From the calculated density profiles obtained previously, we note that there is no unique definition of the film thickness. Following the theme of Gibbs for a single interface as extended to thin films,<sup>38</sup> we construct two dividing surfaces corresponding to the two film/vapor interfaces and define the film thickness as the distance between the two dividing surfaces. In other words, the dividing surfaces separate the (hypothetical) fluid regions of uniform densities. We elaborate upon these hypothetical uniform densities shortly. For a single-component system, there is zero adsorption at the dividing surfaces. Moreover, the total number of particles obtained using this definition must be equal to the total number of particles in the simulation. Thus, the film thickness is given by

$$h^* = \frac{N/A^* - \rho_v^* L_z^*}{\rho_1^* - \rho_v^*} \quad (4)$$

where  $A^*$  is the (nondimensional) cross-sectional area of the simulation box,  $L_z^*$  is the box length in the  $z$  direction,  $\rho_1^*$  is a homogeneous liquid density between the two dividing surfaces, and  $\rho_v^*$  is the homogeneous vapor density. An obvious choice for  $\rho_v^*$  is the simulated uniform vapor density far from the interface. However, the liquid part of the film is not homogeneous anywhere. Thus, the choice of  $\rho_1^*$  is not clear. Following the extended Gibbs convention, we take  $\rho_1^*$  as the density of the liquid in contact with the film through the meniscus,<sup>38</sup> as obtained from the LJ EOS. Table 1 displays the initial and the final film thicknesses in the last two columns for all the films.

In classical Hamaker theory where intermolecular interactions are due solely to the London–van der Waals potential, the force between two surfaces separated by a distance  $h$  varies as  $1/h^3$ .<sup>22</sup> This result translates into the same separation dependence of the disjoining pressure on thickness in the van der Waals part of the theory of Derjaguin, Landau, Verwey, and Overbeek (DLVO),<sup>39</sup> or

$$\Pi = -\frac{A_H}{6\pi h^3} \quad (5)$$

where  $A_H$  is the Hamaker constant. Thus, from eq 5 the slope of the line fitting  $\Pi$  as a function of  $1/h^3$  obtained from the simulations gives  $A_H$ . Figure 7 depicts  $\Pi^*$  as a function of  $1/h^{*3}$  for the two temperatures simulated. Closed diamonds ( $T^* = 0.85$ ) and closed squares ( $T^* = 0.9$ ) represent the simulated values, and the straight lines represent the two fits. Error bars in the value of  $\Pi^*$  are obtained from the errors in calculated values of the normal pressure and the chemical potential for the various films. As we observe from the figure,  $\Pi$  closely varies as  $1/h^3$  for the range of film thickness considered. Accordingly, best straight line fits give at  $T^* = 0.85$ ,  $A_H^* = 161.5$ , and at  $T^* = 0.9$ ,  $A_H^* = 257.6$ . However, lack of calculation precision precludes determination of a temperature



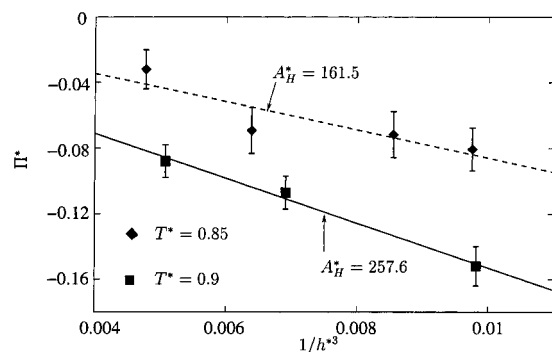


**Figure 7.**  $\Pi$  as a function of  $1/h^3$  as obtained from MD for two different temperatures.

dependence for  $A_H$ . There is, nevertheless, a definite increase in  $\Pi$  as a function of film thickness with temperature. This increase indicates that the change in chemical potential from its bulk coexistence value (where  $\Pi = 0$ ) is more sensitive to the change in film thickness at a higher temperature. For example, films 4 and 9 (at  $T^* = 0.9$  and  $T^* = 0.85$ , respectively) have approximately the same thickness. However, the change in chemical potential from its saturation value for film 4 is about twice as large as that for film 9 (cf. Table 1).

**Comparison to Hamaker Theory.** For a symmetric system of two identical media interacting across another medium, the nondimensional Hamaker constant is<sup>6</sup>

$$A_H^* = 4\pi^2(\rho_1^* - \rho_2^*)^2 \quad (6)$$

where the subscripts (1 and 2) refer to the two distinct media in the system. For  $T^* = 0.9$ , upon using the bulk coexistence densities in eq 6,  $A_H^* = 21.5$ , and for  $T^* = 0.85$ ,  $A_H^* = 23.1$ . Although the densities used in eq 6 for each film thickness must be the liquid and vapor densities at the same chemical potential (that are different than those at bulk coexistence), using the coexistence densities does not change  $A_H$  appreciably. The important assumptions in eqs 5 and 6 are that the free energy of the film system is approximated by the internal energy (thus, giving a zero-temperature description), the structure of the fluid is neglected, and the density of each medium is assumed to be constant up to the interfaces.

A somewhat more quantitative expression for the Hamaker constant is given by Lifshitz theory<sup>22</sup>

$$A_H = \frac{3}{4}kT\left(\frac{\epsilon_1 - \epsilon_2}{\epsilon_1 + \epsilon_2}\right)^2 + \frac{3\pi\hbar\nu_e}{8\sqrt{2}}\frac{(n_1^2 - n_2^2)^2}{(n_1^2 + n_2^2)^{3/2}} \quad (7)$$

where the subscripts 1 and 2, again, refer to the two types of media,  $k$  is Boltzmann's constant,  $\hbar$  is Planck's constant divided by  $2\pi$ ,  $\epsilon_i$  is the dielectric constant of medium  $i$ ,  $n_i$  is the refractive index, and  $\nu_e$  is the first electronic absorption frequency. For vapor,  $\epsilon_i$  and  $n_i$  are close to 1, whereas for the liquid medium, argon properties are used at the temperature of interest. Also,  $\nu_e$  is about  $3 \times 10^{15} \text{ s}^{-1}$  for various materials.<sup>22</sup> From eq 7 and using the properties of liquid argon at  $T^* = 0.9$ ,  $A_H^* = 10.1$ . Although this value of  $A_H$  is smaller than that obtained by standard Hamaker theory, the difference is not of particular importance. Hence, we adopt the definition of  $A_H$  given in eq 6 and compare only to Hamaker theory hereafter.

A striking feature apparent from the preceding discussion is that, with the given definition of the film thickness and the range of the disjoining pressure considered, the Hamaker constant

calculated from the MD simulations differs from the theoretical values by an order of magnitude. A major difference between the theoretical calculations and the simulation is that the Hamaker theory adopts homogeneous fluid properties up to the interfaces (i.e., a slab). Additionally, it assumes that the fluid is structureless and neglects the entropy contribution. Thus, our results show a marked importance of the density profile and the fluid structure. Although it may be possible to redefine arbitrarily the film thickness and obtain a closer match to the theoretical predictions, the effect of the density profile and the fluid structure cannot be discounted. To address this issue more carefully, we employ a density-functional theory that uses an approximate fluid structure and a consistent density profile to calculate the disjoining-pressure isotherm.

**Comparison to Density-Functional Theory.** The equilibrium density profile in the film system is obtained by minimizing the grand-potential free-energy functional,<sup>40</sup>

$$\Omega[\rho(\mathbf{r})] = F[\rho(\mathbf{r})] - \mu \int \rho(\mathbf{r}) d\mathbf{r} \quad (8)$$

where  $F$  is the Helmholtz free-energy functional and  $\mu$  is, again, the chemical potential. Alternately, minimizing  $\Omega$  in eq 8 can be interpreted as minimizing the free energy with the constraint that the number of particles remains constant. In other words,  $\mu$  is a Lagrange multiplier to enforce that constraint. Later, this second interpretation proves useful for interpreting our calculations.

To evaluate the free-energy functional  $F$  in eq 8 we use a density-functional theory in perturbation-theory format (DFT-PT). In DFT-PT, the interparticle potential energy is apportioned into a repulsive part ( $u_0$ ) and an attractive part ( $u_a$ ),

$$u(\mathbf{r}_1, \mathbf{r}_2; \lambda) = u_0(\mathbf{r}_1, \mathbf{r}_2) + \lambda u_a(\mathbf{r}_1, \mathbf{r}_2); \quad 0 \leq \lambda \leq 1 \quad (9)$$

where  $\lambda$  is a coupling parameter and  $\mathbf{r}_i$  is the position of particle  $i$ . For  $\lambda = 1$ , eq 9 gives the full LJ potential. Next, we use the local-density approximation (LDA) and the assumption that the fluid structure is determined solely by the repulsive part of the intermolecular potential. These assumptions are discussed in more detail in Appendix B. Here we present the final result of the functional minimization of the grand potential, or

$$\mu = \mu_0(\rho(\mathbf{r}_1)) + \int d\mathbf{r}_2 \rho(\mathbf{r}_2) g_0(r_{12}; \bar{\rho}) u_a(r_{12}) + \frac{1}{2} \rho(\mathbf{r}_1) \int d\mathbf{r}_2 \rho(\mathbf{r}_2) \frac{\partial g_0(r_{12}; \bar{\rho})}{\partial \bar{\rho}} u_a(r_{12}) \quad (10)$$

where  $\mu_0$  is the chemical potential of the purely repulsive fluid,  $g_0$  is the density-dependent radial distribution function of the purely repulsive fluid,  $\bar{\rho}$  is the arithmetic mean of the densities at positions  $\mathbf{r}_1$  and  $\mathbf{r}_2$ , and  $r_{12} = |\mathbf{r}_1 - \mathbf{r}_2|$ . This equation is similar to that derived by Wadewitz and Winklemann,<sup>25</sup> except that we have used the local density  $\rho(\mathbf{r})$  instead of a coarse-grained density.

To calculate numerically the density profile, we must specify the separation of the interaction potential in eq 9, and also a method to calculate the repulsive radial distribution function  $g_0$ . These issues are discussed in some detail in Appendix C. The repulsive and the attractive components of the interaction potential in eq 9, are segmented according to the prescription of Weeks, Chandler, and Anderson (WCA).<sup>41,42</sup>

At this point, it is useful to specialize some of the above development to homogeneous fluids. Equation 10, for a

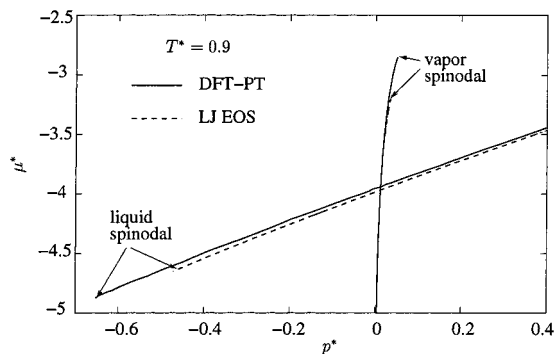


**Figure 8.** The  $\mu$ - $p$  phase diagram for a Lennard-Jones fluid at  $T^* = 0.9$  according to DFT-PT (solid lines) and LJ EOS (dashed lines). The liquid and vapor spinodal points are also demarked for both approaches.

homogeneous fluid, becomes

$$\mu = \mu_0(\rho) + \rho \int d\mathbf{r} g_0(r_{12}; \rho) u_a(r_{12}) + \frac{1}{2} \rho^2 \int d\mathbf{r} \frac{\partial g_0(r_{12}; \rho)}{\partial \rho} u_a(r_{12}) \quad (11)$$

Additionally, from the corresponding homogeneous result for the free energy (cf., eq B2), the homogeneous pressure can be obtained by differentiation. The result is

$$p = p_0(\rho) + \frac{1}{2} \rho^2 \int d\mathbf{r} g_0(r_{12}; \rho) u_a(r_{12}) + \frac{1}{2} \rho^3 \int d\mathbf{r} \frac{\partial g_0(r_{12}; \rho)}{\partial \rho} u_a(r_{12}) \quad (12)$$

where  $p_0$  is the pressure of the homogeneous purely repulsive fluid at density  $\rho$ . Equations 11 and 12 are necessary in determining the disjoining pressure as a function of the chemical potential, as previously discussed. With this approach for evaluating  $\Pi(\mu)$ , instead of using the published LJ EOS<sup>36</sup> (cf. Figure 2), we remain consistent with the framework of DFT-PT.

Thus, we construct the  $\mu$ - $p$  phase diagram from eqs 11 and 12, as shown in Figure 8 for  $T^* = 0.9$ . Solid lines represent the liquid and vapor lines as labeled, whereas dashed lines represent the LJ-EOS results of Figure 2. As clear from Figure 8, agreement between DFT-PT and the exact result is quite good. In fact, the reduced bulk-coexistence densities from DFT-PT are 0.763 for the liquid and 0.0141 for the vapor, as compared to 0.752 and 0.015 from the LJ EOS. Similarly, DFT-PT gives  $\mu^* = -3.938$  and  $p^* = 0.01197$  at coexistence compared to  $\mu^* = -3.962$  and  $p^* = 0.01137$  from the LJ EOS (cf. Table 1). This agreement deteriorates at intermediate densities (i.e., for those regions near the vapor and liquid spinodals). Also, spinodal regions (that lie in these intermediate density regions) are incorrectly represented. Hence, we expect the density profile calculated from DFT-PT to be somewhat different from the actual density profiles obtained from MD.

To establish the density profile, we rewrite eq 10 for a cylindrical axisymmetric film with interfaces perpendicular to the  $z$ -direction as

$$\begin{aligned} \mu_0(\rho(z_1)) = \mu - & 2\pi \int_{z_1-r_c}^{z_1+r_c} dz_2 \rho(z_2) \int_{|z_1-z_2|}^{r_c} dr_{12} r_{12} u_a(r_{12}) g_0(r_{12}; \bar{\rho}(z_1, z_2)) - \\ & \pi \rho(z_1) \int_{z_1-r_c}^{z_1+r_c} dz_2 \rho(z_2) \int_{|z_1-z_2|}^{r_c} dr_{12} r_{12} u_a(r_{12}) \frac{\partial g_0(r_{12}; \bar{\rho}(z_1, z_2))}{\partial \bar{\rho}} \end{aligned} \quad (13)$$

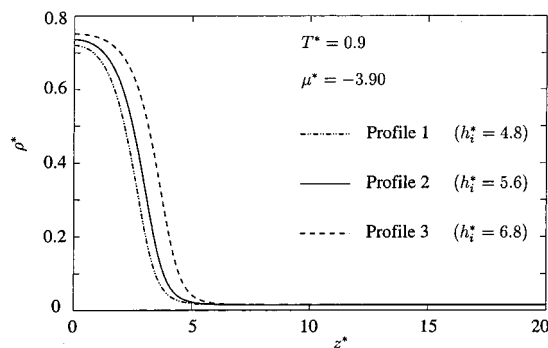


**Figure 9.** Density profiles for three different values of the initial film thickness for  $\mu^* = -3.90$  from DFT-PT.

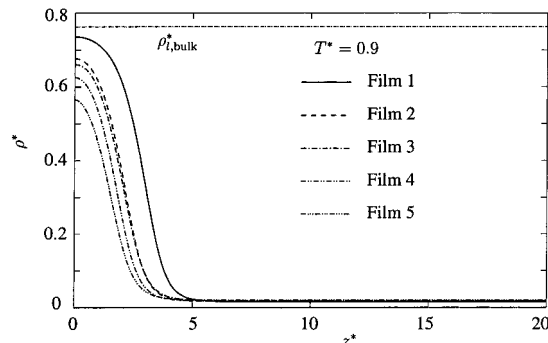


**Figure 10.** Density profiles for films 1–5 from DFT-PT at  $T^* = 0.9$  in Table 2.

where we have introduced  $r_c$  as the potential cut off. The total  $z$  length is chosen as  $20\sigma$  (the same as that in MD due to symmetry about  $z = 0$ ), and the density profile is discretized along the  $z$ -axis by  $0.1\sigma$ . In other words,  $z_1^*$  changes from 0 to 20 in our calculations, and  $z_1^*$  from  $-20$  to 0 follows from symmetry. Equation 13 is solved iteratively with an initial guess of a step-function profile (from the bulk coexistence densities). Given a value of  $\mu$  (in the metastable vapor region), we solve the right side of eq 13 to obtain  $\mu_0(\rho(z_1))$ . Since  $\mu_0$  is a monotonic function of  $\rho$ ,  $\mu_0(\rho(z_1))$  is easily inverted to obtained  $\rho(z_1)$ . Subsequently, this new  $\rho(z_1)$  is used in the right side of eq 13 for the next iteration.

We remark that the thickness of the initial step-function density profile (i.e., the initial width of the liquid part from  $z = 0$ ) is not determined a priori. To illustrate this, Figure 9 depicts the final iterated density profile at  $\mu^* = -3.90$  for three different values of the initial half width of the step profile ( $h_i/2$ , as defined previously in MD simulations, or, equivalently, the initial number of particles). For profile 1,  $h_i^*/2 = 2.4$ ; for profile 2, it is 2.8; and for profile 3, it is 3.4. Clearly, these three converged profiles represent distinct cases at the same  $\mu$ . To determine the required density profile at a particular  $\mu$ , we turn to the alternate interpretation of minimizing  $F$  with the constraint that the number of particles (or, the area under the  $\rho(z)$  curve) be the same as in the initial profile. Of these three profiles, only profile 2 satisfies this constant-mass constraint. For profile 1, the area under the curve is less than the area under the initial curve, and vice versa for profile 3. That is, eq 13 is resolved for different initial slab density profiles until the initial-guess slab profile and the final converged profile exhibit the same mass.

Density profiles from DFT-PT for a range of  $\mu$  values are shown in Figure 10 for five different films. The liquid coexistence density  $\rho_{i,bulk}$  is also labeled for reference. Although we cannot directly compare these results with the MD results

**TABLE 2: Relevant Quantities Calculated Using DFT-PT for All the Films  $T^* = 0.9$** 

film	$\mu^*$	$N/A^*$	$\rho_v^*$	$\Pi^*$	$h_i^*$	$h^*$
1	-3.90	4.675	0.01498	-0.0281	5.6	5.429
2	-3.86	3.330	0.01557	-0.0576	3.8	3.597
3	-3.80	3.032	0.01681	-0.1033	3.4	3.122
4	-3.75	2.882	0.01794	-0.1416	3.0	2.856
5	-3.70	2.584	0.01916	-0.1788	2.6	2.391

(since  $\mu$  is not exactly equivalent in both), Figure 10 displays very similar features to those in Figure 3. More precisely, the densities at the center of the films are lower than the bulk coexistence density. Nevertheless, we expect quantitative differences between the corresponding results due to approximations made in DFT-PT. In particular, although the range of  $\mu$  values is similar in both Figures 3 and 10, the films in Figure 10 appear to be thinner.

$\Pi^*$  is now calculated directly from the phase diagram of Figure 8, and  $h^*$  is calculated as discussed previously for MD. For thinner films, it is difficult to obtain a converged solution for the density profile (i.e., a finer grid than  $\Delta z^* = 0.1$  is needed to obtain a solution other than that of uniform vapor density). For thicker films,  $\mu$  is very close to the bulk coexistence value, and the small difference between the film and the saturation chemical potential is overshadowed by discretization errors (thus, again, requiring a finer  $z$ -grid to obtain a wider range of film thicknesses). Table 2 shows all relevant calculated quantities of the intermediate thickness thin DFT-PT films.

$\Pi^*$  as a function of  $1/h^{*3}$  at  $T^* = 0.9$ , as obtained from DFT-PT, is depicted in Figure 11 as solid diamonds. In addition, results from MD (solid squares) at that temperature (cf., Figure 7) and those from Hamaker theory (solid line for a slab profile and the Hamaker constant calculated from eq 6) are shown for comparison. Clearly, DFT-PT, which uses a density profile and an approximate structure of the fluid, is much closer to the MD results than is Hamaker theory. This is expected since the classical Hamaker theory neglects fluid structure and entropy completely, and assumes a slab density profile. Conversely, the difference between DFT-PT and MD is due to the fact that the pair correlation function used in DFT-PT is not strictly correct. This error has an effect both on  $\Pi(\mu)$  and the density profile, and hence, on the film thickness.

An important feature of DFT-PT in Figure 11 is that  $\Pi$  does not vary as the inverse cube of film thickness over a large range of film thickness. This result is not surprising since the  $1/h^3$  functional dependence is suggested by the Hamaker slab-profile theory that itself is in large error. We additionally performed calculations of density profiles for various films (for particular values of  $\mu$ ) using a density-gradient theory.<sup>40</sup> In the density-gradient theory, a differential equation is obtained for the density profile as a function of  $z$ , and the free energy (or the chemical potential) is related to the derivatives of the density with respect to  $z$  via a density-dependent influence parameter.<sup>40</sup>  $\Pi$  as a function of  $\mu$  was, again, obtained from the phase diagram. Results for the density-gradient theory are similar to the results from DFT-PT. In particular, density-gradient theory also reveals that  $\Pi$  does not strictly vary as the inverse cube of film thickness. Moreover, we are able to calculate disjoining pressures for a larger range of film thicknesses using the density-gradient theory, so the lack of an inverse-cube dependence is more pronounced, especially the bending over that is depicted by films 1 and 5 of DFT-PT in Table 2 (cf. the two extreme DFT-PT points in Figure 11). Thus, it is possible that at larger film thickness all theories approach that of Hamaker. Unfortunately, our MD and DFT-PT calculations lack the precision to

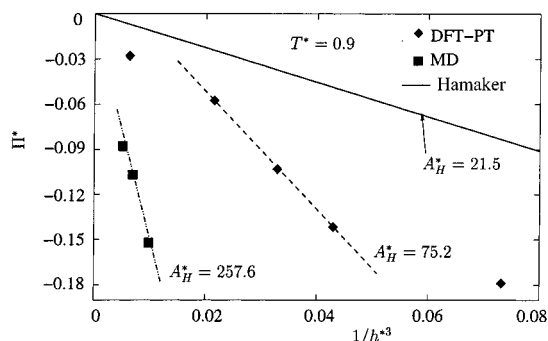


**Figure 11.** Comparison of the disjoining-pressure isotherm at  $T^* = 0.9$  as obtained from MD, DFT-PT, and Hamaker theory. Straight-line fits to the MD results (dot-dashed line) and the middle three points from DFT-PT (dashed line) that are in the range of MD  $\Pi$  values are also shown, along with the respective values of the Hamaker constant.

investigate this asymptotic limit. Some effort has been directed to this case, albeit approximate.<sup>43</sup>

Despite the fact that DFT-PT and the density-gradient theory suggest a non- $1/h^3$  dependence for  $\Pi$ , we calculate an apparent Hamaker constant from DFT-PT in the range of  $\Pi$  values obtained from MD (namely, from films 2–4 of DFT-PT). The slope of the dashed line in Figure 11 leads to  $A_H^* = 75.2$ . Compared to the MD result of 257.6 and the Hamaker-theory result of 21.5, the DFT-PT result reflects the point made previously that upon removing the severe assumptions made in Hamaker theory (namely, that the fluid is structureless, the density profile is a slab, and the free energy is approximated by the internal energy) we obtain a result much closer to MD. The remaining difference between DFT-PT and MD is due to the approximate fluid structure used in DFT-PT. Nevertheless, there remains a significant difference between DFT-PT and MD, mainly because of the difference in respective density profiles that result from the use of approximate structure in DFT-PT and the subsequently calculated film thickness. In fact, as is clear from Figure 8,  $\Pi(\mu)$  from both DFT-PT and the LJ EOS (or, equivalently, MD) are quite close.

## Conclusions

For the first time, we present MD simulations of Lennard-Jones free thin films to calculate disjoining-pressure isotherms. First, the normal component of the pressure tensor and the chemical potential of the thin-film system are evaluated. Then, to obtain the liquid properties at the same chemical potential, we simulate a film thick enough to correspond to bulk liquid/vapor coexistence, calculate its normal pressure and chemical potential, and integrate the Gibbs–Duhem equation between the saturation and the film chemical potential. We confirm that the thin-film system is indistinguishable from the metastable homogeneous vapor line in the  $\mu$ - $p$  phase diagram; this allows the direct calculation of the disjoining pressure as a function of the chemical potential for systems whose phase diagram is available.

Since the disjoining pressure is reported in the literature as a function of the film thickness, we use a Gibbsian-motivated definition of the film thickness prevalent in the literature. This definition leads to a comparison with classical Hamaker theory that is based on a slab density profile and a structureless fluid exhibiting only internal energy. We find that the disjoining pressure obtained from MD at any film thickness is dramatically larger in magnitude than that obtained from the Hamaker theory of van der Waals forces. In particular, the value of the Hamaker constant is about an order of magnitude larger at either

temperature simulated in MD compared to the classical Hamaker theory. To understand this difference, we also use density-functional theory to calculate the disjoining-pressure isotherm. In DFT-PT, the assumption of a structureless and zero-entropy fluid is relaxed, the structure is approximated by an equivalent hard-sphere fluid, and the density profile is calculated consistently. We find that DFT-PT gives a remarkably better description of the disjoining-pressure isotherm, much closer to the result from MD than is Hamaker theory. The difference between DFT-PT and MD simulation is attributed to the approximation of the fluid structure. Although in this work we study only Lennard-Jones particles, the outlined methodology is applicable to more realistic thin-film systems.

**Acknowledgment.** This work was partially funded by the Assistant Secretary for Fossil Energy, Office of Oil, Gas, and Shale Technologies of the U.S. Department of Energy under Contract DE-AC03-76SF00098 to the Lawrence Berkeley National Laboratory of the University of California.

### Appendix A: Error in $\Pi$ due to the Neglect of Change of Liquid Density with Pressure

We estimate here the effect of the constant-liquid-density approximation (cf. eq 3) on quantifying  $\Pi$ . Upon integrating  $\rho^*$  with respect to  $\mu^*$  by parts from the saturation-state chemical potential to that required, we obtain

$$\int_{\mu_{\text{sat}}^*}^{\mu^*} \rho^* d\mu^* = \rho^* \mu^* - \rho_{\text{sat}}^* \mu_{\text{sat}}^* - \int_{\rho_{\text{sat}}^*}^{\rho^*} \mu^* d\rho^* \quad (\text{A1})$$

Thus, to calculate the disjoining pressure rigorously, the right side of eq 3 must be replaced by the right side of eq A1. From the LJ EOS, we compute the required correction. Thus, for film 4 from MD, the value of disjoining pressure obtained upon taking the above-mentioned correction into account is 0.154. In other words, the correction is extremely minor, and we can safely use eq 3. Otherwise, to obtain the value of the exact disjoining pressure without any reference to the published LJ EOS, we must simulate intermediate liquid densities between  $\rho_1^*$  and  $\rho_{\text{sat}}^*$ .

### Appendix B: Density-Functional Theory

For inhomogeneous fluids, eq 9 leads to the exact free energy as a functional of the density profile  $\rho(\mathbf{r})$ , giving<sup>23–25</sup>

$$F[\rho(\mathbf{r})] = F_0[\rho(\mathbf{r})] + \frac{1}{2} \int_0^1 d\lambda \int d\mathbf{r}_1 \rho(\mathbf{r}_1) \int d\mathbf{r}_2 \rho(\mathbf{r}_2) g(\mathbf{r}_1, \mathbf{r}_2; \lambda) u_a(\mathbf{r}_1, \mathbf{r}_2) \quad (\text{B1})$$

where  $F_0$  is the part of the free energy due to the repulsive potential  $u_0$  and the ideal gas, and  $g$  is the  $\lambda$ -dependent pair distribution function of the inhomogeneous fluid. With the assumption that the structure of a fluid is determined solely by repulsive intermolecular forces, the  $\lambda$  integration is done trivially to yield

$$F[\rho(\mathbf{r})] = F_0[\rho(\mathbf{r})] + \frac{1}{2} \int d\mathbf{r}_1 \rho(\mathbf{r}_1) \int d\mathbf{r}_2 \rho(\mathbf{r}_2) g_0(\mathbf{r}_1, \mathbf{r}_2; \rho) u_a(\mathbf{r}_1, \mathbf{r}_2) \quad (\text{B2})$$

where  $g_0$  is the density-dependent pair distribution function of the inhomogeneous fluid solely due to the repulsive part of the interaction potential.

The above-mentioned assumption is very good at high liquid densities, but introduces errors at lower densities.<sup>41,42</sup> However,

this is the simplest assumption that one can make without characterizing the fluid as completely structureless. Another assumption usually introduced at this point is that the pair distribution function of the inhomogeneous fluid is the radial distribution function of a homogeneous fluid at some appropriate mean density, or<sup>25,44</sup>

$$g_0(\mathbf{r}_1, \mathbf{r}_2; \rho) = g_0(r_{12}; \bar{\rho}) \quad (\text{B3})$$

where, within the local density approximation (LDA),<sup>24,40</sup> the average density  $\bar{\rho}$  is

$$\bar{\rho} = \frac{1}{2}(\rho(\mathbf{r}_1) + \rho(\mathbf{r}_2)) \quad (\text{B4})$$

Although LDA is not suitable for interfaces with strong inhomogeneity (e.g., the solid/liquid interface),<sup>24,40,45</sup> it is adequate for liquid/vapor interfaces.<sup>40</sup> Also, within LDA, for fluids interacting only with short-ranged repulsive potentials, the total free energy is<sup>24,40,46</sup>

$$F_0[\rho] \approx \int d\mathbf{r} \rho(\mathbf{r}) f_0(\rho(\mathbf{r})) \quad (\text{B5})$$

where  $f_0$  is the local free-energy density of the repulsive part of the interparticle potential. This purely repulsive fluid exists at all densities up to the crystallization density. Thus, its properties, such as the chemical potential and pressure, are well defined. With eqs B3–B5, functional minimization of the grand-potential functional in eq 8 yields eq 10 of the text.

### Appendix C: The Repulsive Part of the Intermolecular Potential

As mentioned in the text, we use the WCA prescription to split the intermolecular potential. Instead of the full LJ potential, we use the same truncated and shifted LJ potential (at  $r_c = 6.5\sigma$ ) as that in MD simulations. The repulsive part is

$$u_0(r) = \begin{cases} u(r) + \epsilon; & r \leq r_0 \\ 0; & r > r_0 \end{cases} \quad (\text{C1})$$

where  $u(r)$  is the cut and shifted LJ potential and  $r_0 = 2^{1/6}\sigma$  is the position of the minimum of  $u(r)$  or the LJ potential. Further,  $u_a = u - u_0$ . Finally, the repulsive part of the LJ potential is approximated by a hard-sphere fluid with an appropriately chosen hard-sphere diameter. This equivalent hard-sphere diameter is a function of temperature and a weak function of density as calculated in the prescription of WCA to minimize the difference between the free energy calculated using the hard-sphere fluid and the repulsive LJ fluid. However, for simplicity, we choose a density-independent hard-sphere diameter  $d$  according to the Barker and Henderson prescription,<sup>47</sup>

$$d = \int_0^{r_0} (1 - \exp^{-\beta u_0(r)}) dr \quad (\text{C2})$$

where  $\beta$  is  $1/kT$ .

With the hard-sphere diameter chosen in eq C2, the density-dependent radial distribution function for the hard-sphere fluid is calculated from the Percus–Yevick (PY) theory.<sup>48–50</sup> Similarly, the density derivative of the radial distribution function can be calculated.<sup>50</sup> Thus,  $\mu_0$  in eqs 10 and 11 and  $p_0$  in eq 12 are the hard-sphere chemical potential and pressure that are



monotonic functions of density. We choose the Carnahan and Starling equation of state for these hard-sphere properties.<sup>51</sup>

## References and Notes

- (1) Davis, H. T.; Scriven, L. E. *Adv. Chem. Phys.* **1982**, 49, 357.
- (2) Derjaguin, B. V.; Churaev, N. V. *Colloid J. USSR* **1976**, 38, 402.
- (3) Derjaguin, B. V.; Churaev, N. V. *J. Colloid Interface Sci.* **1978**, 66, 389.
- (4) Kruglyakov, P. M. *Thin Liquid Films*; Ivanov, I. B., Ed.; Marcel Dekker: New York, 1988; Chapter 11, p 767.
- (5) Ivanov, I. B. *Colloids Surf. A* **1997**, 128, 155.
- (6) Hamaker, H. C. *Phys. IV* **1937**, 10, 1058.
- (7) Ninham, B. W.; Parsegian, V. A.; Weiss, G. H. *J. Stat. Phys.* **1970**, 2, 323.
- (8) Mysels, K. J.; Jones, M. N. *Discuss. Faraday Soc.* **1966**, 42, 42.
- (9) Exerowa, D.; Kolarov, T.; Khristov, K. H. R. *Colloids Surf.* **1989**, 22, 171.
- (10) Kolarov, T.; Cohen, R.; Exerowa, D. *Colloids Surf.* **1989**, 42, 49.
- (11) Bergeron, V.; Radke, C. J. *Langmuir* **1992**, 8, 3020.
- (12) Sedev, R.; Nemeth, Z.; Ivanova, R.; Exerowa, D. *Colloids Surf. A* **1999**, 149, 141.
- (13) Cascao Pereira, L. G.; Johansson, C.; Blanch, H. W.; Radke, C. J. *Colloids Surf. A* **2001**, 186, 103.
- (14) Bergeron, V.; Langevin, D.; Asnacios, A. *Langmuir* **1996**, 12, 1550.
- (15) Gallego, L. J.; Rey, C.; Grimson, M. J. *Mol. Phys.* **1991**, 74, 383.
- (16) Magda, J. J.; Tirrell, M.; Davis, H. T. *J. Chem. Phys.* **1985**, 83, 1888.
- (17) Dickman, R.; Anderson, P. E. *J. Chem. Phys.* **1993**, 99, 3112.
- (18) Jimenez, J.; Rajagopalan, R. *Eur. Phys. J. B* **1998**, 5, 237.
- (19) Weng, J.-G.; Park, S.; Lukes, J. R.; Tien, C.-L. *J. Chem. Phys.* **2000**, 113, 5917.
- (20) Chambers, K. T.; Radke, C. J. *Interfacial Phenomena in Petroleum Recovery*; Morrow, N. R., Ed.; Marcel Dekker Inc.: New York, 1990; p 211.
- (21) Mahanty, J.; Ninham, B. W. *Dispersion Forces*; Academic Press: New York, 1976.
- (22) Israelachvili, J. N. *Intermolecular and Surface Forces*; Academic Press: New York, 1991; Chapters 6, 11.
- (23) Tang, Z.; Scriven, L. E.; Davis, H. T. *J. Chem. Phys.* **1991**, 95, 2659.
- (24) Tarazona, P.; Marconi, U. M. B.; Evans, R. *Mol. Phys.* **1987**, 60, 573.
- (25) Wadewitz, T.; Winkelmann, J. *J. Chem. Phys.* **2000**, 113, 2447.
- (26) Trokhymchuk, A.; Alejandre, J. *J. Chem. Phys.* **1999**, 111, 8510.
- (27) Chen, L. J. *J. Chem. Phys.* **1995**, 103, 10214.
- (28) Nose, S. *Mol. Phys.* **1984**, 52, 255.
- (29) Hoover, W. G. *Phys. Rev. A* **1985**, 31, 1695.
- (30) Frenkel, D.; Smit, B. *Understanding Molecular Simulations*; Academic Press: New York, 1991; Chapter 6.
- (31) Allen, M. P.; Tildesley, D. J. *Computer Simulation of Liquids*; Clarendon Press: Oxford, 1987; Chapter 7.
- (32) Irving, J. H.; Kirkwood, J. G. *J. Chem. Phys.* **1950**, 18, 817.
- (33) Walton, J. P. R. B.; Tildesley, D. J.; Rowlinson, J. S. *Mol. Phys.* **1983**, 48, 1357.
- (34) Winter, S. J. Ph.D. Dissertation, University of California: Berkeley, 1999; Chapter 3.
- (35) Widom, B. *Journal of Statistical Physics* **1978**, 19, 563.
- (36) Johnson, J. K.; Zollweg, J. A.; Gubbins, K. E. *Mol. Phys.* **1993**, 78, 591.
- (37) Smit, B. *J. Chem. Phys.* **1992**, 96, 8639.
- (38) de Feijter, J. A. *Thin Liquid Films*; Ivanov, I. B., Ed.; Markel Dekker: New York, 1988; Chapter 1.
- (39) Overbeek, J. Th. G. *Colloid Science I*; Kruyt, H. R., Ed.; Elsevier: Amsterdam, 1952; Chapter 6.
- (40) Davis, H. T. *Statistical Mechanics of Phases, Interfaces, and Thin Films*; VCH: New York, 1996; Chapter 11.
- (41) Weeks, J. D.; Chandler, D.; Anderson, H. C. *J. Chem. Phys.* **1971**, 54, 5237.
- (42) Chandler, D.; Weeks, J. D.; Anderson, H. C. *Science* **1983**, 220, 787.
- (43) Trofimova, E. N.; Kuni, F. M.; Rusanov, A. I. *Colloid J.—USSR* **1969**, 31, 458.
- (44) Sokolowski, J.; Fischer, J. *J. Chem. Phys.* **1992**, 96, 5441.
- (45) Peterson, B. K.; Gubbins, K. E.; Heffelfinger, G. S.; Marconi, U. M. B.; van Swol, F. *J. Chem. Phys.* **1988**, 88, 6487.
- (46) Sullivan, D. E. *J. Chem. Phys.* **1981**, 74, 2604.
- (47) Barker, J. A.; Henderson, D. *J. Chem. Phys.* **1967**, 47, 4714.
- (48) Wertheim, M. S. *Phys. Rev. Lett.* **1963**, 10, 321.
- (49) Thiele, E. *J. Chem. Phys.* **1963**, 39, 474.
- (50) Chandler, D. *Chemistry 220 B Lecture Notes*; University of California: Berkeley: Berkeley, Fall 2000.
- (51) Carnahan, N. F.; Starling, K. E. *J. Chem. Phys.* **1969**, 51, 635.